Simulation of monolithic active pixel sensor with high resistivity epitaxial layer

FU Min TANG Zhenan*

School of Electronic Science and Technology, Dalian University of Technology, Dalian 116024, China

Abstract The time and efficiency of charge collection are the key factors of monolithic active pixel sensor devices for minimum ionizing particles tracking detection. In this paper, 3D models of pixels with different resistivity epitaxial layers (epi-layers) are built and simulated using Synopsys-Sentaurus. The basic characteristics of detectors are evaluated, including electric potential, electric field, and depleted region. Results indicate that the high resistivity (HR) epi-layer is a better choice. Further, simulation results show that the key collection performance is significantly improved owing to a wider and stronger electric field in the N type HR epi-layer.

Key words Monolithic active pixel sensor, Charge collection, High resistivity, Simulation

1 Introduction

A novel detector of minimum ionizing particles (MIP), based on monolithic active pixel sensor (MAPS) of complementary metal-oxide-semiconductor (CMOS) transistor, was proposed by R. Turchetta *et al*.[1] in 2001. Its basic pixel architecture is similar to the visible light CMOS camera sensor, and the readout electronics are integrated into the sensitive volume on the same wafer, allowing almost 100% of fill-factor[2,3]. Considering high quality crystal structure and excellent electric characteristics, the wafer used for MAPS is usually deposited with a 10–20 μm epi-layer as the primary sensitive region[4,5]. A series of minimum ionizing particle MOS active pixel sensor (MIMOSA) chips have been designed, fabricated and tested successfully by Institut Pluridisciplinaire Hubert Curien, France[6–8]. Also, it is illustrated that MAPS can be fabricated in a standard CMOS planar process, providing a low cost and high resolution for MIP detection[9], and in an MAPS pixel, most of the charges generated can be collected by the positive biased N-well, the grounded P-wells, and the substrate.

In this paper, for studying the crucial points of MIP detectors, time and efficiency of charge collection[10], 3D structures of single pixel and 3×3 matrix with similar baselines and epi-layers of different resistivities are built. The physical level semi- conductor device is simulated using the 3D simulator Synopsys-Sentaurus, with the quasi-stationary and transient mode to evaluate the static characteristics, and charge collection performance, which is improved significantly when the epi-layer is high resistive, especially the N type.

2 Simulation tools

The 3D device simulation package with finite element analysis method was first seen in 1981[11], but until several years ago most of the tools were 2D oriented and few physical level semiconductor devices were available. Recently, the tools have become accurate enough to simulate the 3D structures of radiation detectors. Some advanced solid state physics models, e.g. carrier mobility, recombination, magnetic field, temperature dependence and heavy ion particle model, are available in the simulations. In 2008, the commercial simulator Sentaurus package of Synopsys, as the newest generation of computer aided design (TCAD) software, replaced the TCAD of Integrated Systems Engineering (ISE). Also, the subprogram Sentaurus Structure Editor (SSE) and Sentaurus Device (SD) replaced the Mesh-ISE and Dessis-ISE.

* Corresponding author. *E-mail address*: fumin1977@hotmail.com; tangza@dlut.edu.cn

Received date: 2011-03-28

The SSE can be used to interactively describe device structure, and create mesh grids by an embedded meshing algorithm. The SD as a solver can conduct the physical level equations and the results visualized and analyzed by costumed Tecplot or script supported Inspect[12]. On the other hand, because of the rapid development in detector fabrication in the past decade, the 3D structures is becoming increasingly important in understanding the detector behaviors[13,14], and the Sentaurus simulator works perfectly in a 3D mode.

3 Simulation structures

In this paper, we use a compact single pixel for evaluating static characteristics (Fig.1), and a 3×3 pixels matrix for charge collection (Fig.2). The basic frameworks of simulated structures are created referring the design of MIMOSA-26 chip[8]. The pitch size between neighboring collection electrodes is less than 20 μm, and a 3.4 μm × 4.3 μm × 3 μm wedge-like N-well beneath each electrode is plugged in the epi-layer as a probe to collect electrons in adjacent regions generated by charged particles. The N-wells in all pixels are surrounded by P-wells to suppress neighboring diffusion and integrate the associated N-type MOS circuits.

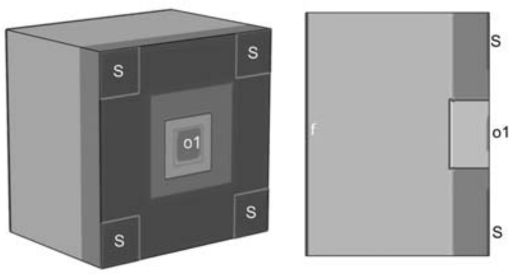

Fig.1 Structure of a single pixel model. The cross section is sliced along middle line of the pixel. o1, collection electrode; S, P-well electrode; f, substrate electrode.

According to G. Deptuch *et al.*[10] and D. Husson[15], a substrate of 30-μm thickness could contribute to the charge collection, but in our simulation the substrate can be further reduced to save computation hours. Without considering neighboring diffusion and substrate contribution in static simulations, the single pixel structure is simplified by removing the substrate but keeping just a 0.3-μm P-type heavily doped layer at the bottom of the epi-layer. The auxiliary parts of silicon around the 3×3 pixels are added, so as to factually emulate the procedure of charge diffusion. The default boundary used in the simulator is an ideal Neumann reflective condition, and all electrons and holes charges generated in the virtual device, except the recombined, are collected. This would cause efficiency overestimating due to collection of the diffused charges, hence the four oxide walls of about 1-μm thick to the whole device volume, so as to avoid the overestimation. At the interfaces between the oxide walls and the silicon bulk, a suitable recombination velocity is defined to consume the charges which need not be collected by the electrodes.

Fig.2 Structure of a 3×3 matrix model. The pixels are surrounded by auxiliary parts of silicon and oxide walls. The o5 is collection electrode of the central pixel.

4 Static simulations

As a main sensitive region, the epi-layer is the key of study. For the single pixel structure, six simulation models of 15-μm epi-layer in the N or P type are constructed, with a 20-μm pitch and a 0.3-μm substrate, in resistivity of 100, 200, or 400 Ω·cm (Table 1). The quasi-stationary mode is used to evaluate the static characteristics of MAPS. As the influential factors for the charge collection, the profiles of electron lifetime, electric field, electric potential and depletion region are shown in the following figures.

Table 1 Simulated pixel structures with a pitch of 20 μm; epi-layer of 15 μm, and substrate of 0.3 μm.

Resistivity / Ω·cm	Type	Concentration / $\times 10^{13}$ cm^{-3}
400	N	1.1
200	N	2.1
100	N	4.2
400	P	3.3
200	P	6.5
100	P	13.0

The electron lifetime can limit the time and the distance of the free charge diffusion. In Fig.3, the curves of doping concentration and electron lifetime are achieved by slicing along the central axis of the pixel. In the epi-layers, corresponding from 0.5 to 11.7 μm in the X axis, the doping concentration is in the range of 1.1×10^{13} to 1.3×10^{14} cm^{-3}; and the resistivity of 400 to 100 Ω·cm; but the electron lifetime from 9.93 to 9.99 μs are obtained by the SD simulator using the doping information without considering unknown defects and traps. Also, the electron lifetime is 10 μs in a 1.0×10^{15} $/cm^3$ doped epi-layer as reported previously[10]. These indicate that changes in resistivity and doping concentration have little effect on the electron lifetime and the additional influence on the charge collection is negligible.

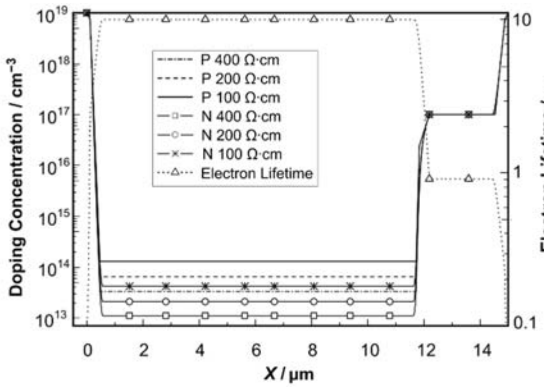

Fig.3 Simulated doping profiles and electron lifetime. The electron lifetimes are almost same at the different doping curves.

The electric potential within the pixel is determined by the fixed voltage on the external contacts or the implanted dopant-related internal potentials, because the Fermi level is dominated by the dopant type and concentration, according to the semiconductor theory. In Fig. 4, in the region of X= 5–10 μm, the potentials of the doped epi-layers vary from –0.3 to 0.9 V, and the gradients are extremely distinct at the electric potentials from 1.2 to –0.5 V. As a result, when the non-equilibrium electrons and holes are injected, separated, and attracted in opposite directions, they are of the same movement trends, despite the different motivations.

The function of electric field and potential is described by the Poisson's equation, $\nabla^2\Phi = -\mathrm{d}E(x)/\mathrm{d}x$, where Φ is electric potential and $E(x)$ is electric field along the X axis. This is verified by the simulation (Fig.5). The peaks of 10 to 13 μm correspond to the potential gradients between the epi-layers and the N-wells. The highest peak is seen with the P type 100 Ω·cm pixel, which has the lowest Fermi level. In the primary part of the epi-layers from 2 to 8 μm, the electric fields of the P type pixels are almost zero, while they are over 500 V/cm in N type pixels, especially the 200–400 Ω·cm pixels.

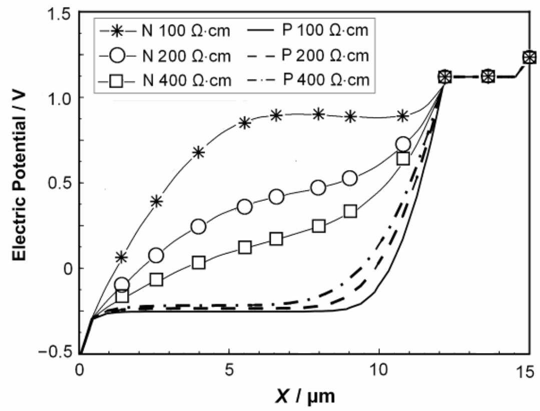

Fig.4 Simulated electric potential profiles. The two ends of the curves are fixed, but the middle parts are altered.

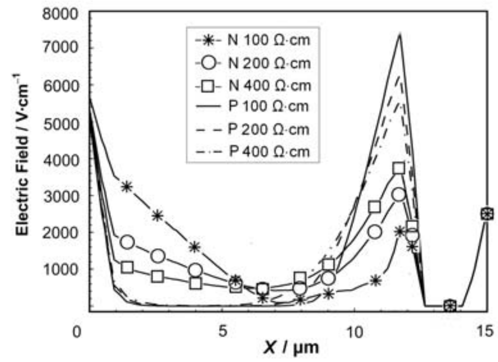

Fig.5 Simulated electric field for the P and N type pixels. The N 400 Ω·cm pixel has the most uniform electric field.

Distribution of the electric potential and the fields are shown in Fig.6. In P type pixels, the distributions of electric potential are relatively uniform in the epi-layers and the contours are compressed near to the N-wells, indicating that the free electrons would move randomly without any inclinations in most parts of the epi-layer, as shown in Fig.6(A-d), (A-e) and (A-f). In N type ones, the contours are distributed all over the epi-layers, and some dome-like potential distributions in the center of the pixels are helpful to collect the electrons of the N-wells, as shown in Fig.6(A-a), (A-b) and (A-c).

Because a strong and wide electric field helps the N-wells to attract the electrons, the range of electric field near the N-well is an influential factor of charge collection. In P type epi-layer, the field is too weak to drive the electrons and holes, but the regions between the N-wells and epi-layers reveal that the higher resistivity leads to a bigger field in Fig.6(B-d), (B-e), and (B-f). In the N type structure, the pixels have better collection performance because of the wider electric field. Fields in middle part of the N type epi-layers are weak, decreasing with the epi- layers thickness, as shown in Fig.6(B-a), (B-b) and (B- c).

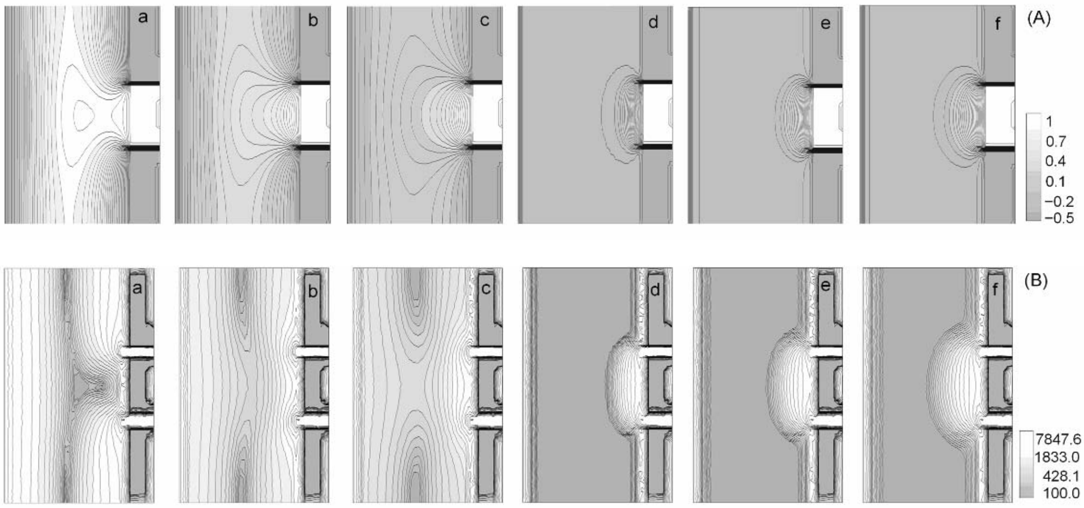

Fig.6 Distribution of the electric potential (A) (in V) and electric field (B) (in V/cm) in pixels.. The potential distribution is almost uniform in most region of the P type epi-layer, but it varies in the N type epi-layer. Obviously, the field in P type epi-layer is too weak to drive electrons to the collection electrode and the primary collection mechanism is only diffusion. (a) N type 100 Ω·cm, (b) N type 200 Ω·cm, (c) N type 400 Ω·cm, (d) P type 100 Ω·cm; (e) P type 200 Ω·cm, and (f) P type 400 Ω·cm.

The depletion region, as shadowed in Fig.7, can reduce recombination and increase collection efficiency. The N type epi-layers have wider depletion regions than the P type, and the layers of higher resistivity are depleted more than those of the lower resistivity. The phenomena can be explained as follows: In the N type epi-layers, the regions are emptied by PN junctions formed by the P++ substrate and the N+ epi-layer, or generated by the P+ well and the N+ epi-layer. Thus, the depleted regions in the N type structures are wider, and small parts of the P type epi-layers are exhausted only within the adjacent volumes of N-wells. Also, compared to the layers of lower resistivity, the higher resistivity layers have less doping concentrations, hence less free electrons generated by impurity and easier depletion.

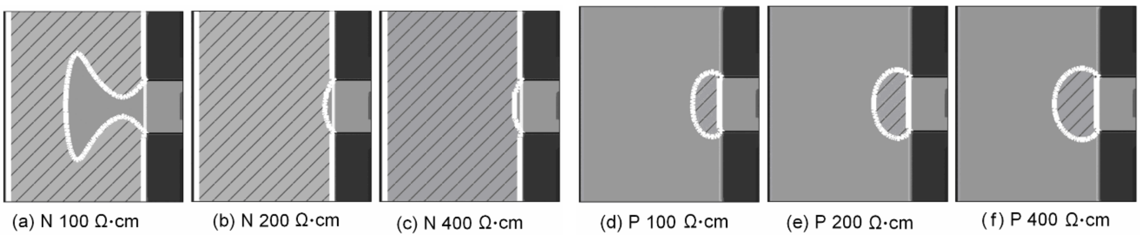

Fig.7 Depletion region (shadowed and surrounded by white lines) of the pixels.

When an epi-layer of high resistivity (HR) is used to replace that of normal resistivity (NR) P type as the sensitive region, the pixel structure becomes a P-intrinsic-N photodiode. Whether the P type or N type is of low enough doping concentration, the HR epi-layer looks as the intrinsic silicon and the interface among the epi-layer, and so do the wells and the substrate, Under the collection mechanism of non-equilibrium, an N type HR epi-layer performs better than the P-type ones in electron collection, hence a potential choice for MAPS collection.

5 Transient simulations

Based on the MIMOSA-26 chips, two P type epi-layers in the matrix structures are constructed: 14-μm thick NR epi-layer of 19 Ω·cm (doped to 7×10^{14} cm^{-3}), and 15-μm thick NR epi-layer of 400 Ω·cm (doped to 3.3×10^{13} /cm^{-3})[16]. In order to evaluate the N type HR epitaxial sensors, another virtual 400 Ω·cm doped device is simulated. All the matrix structures have a 30-μm substrate and 18.4-μm pitch.

Hundreds of modified heavy ion models are added in the simulations independently to eavluate each of the structure under ^{55}Fe irradiation. Considering the symmetry pixel structure and the matrix, a cube within the central pixel is defined as an event region with one quarter of the entire pixel structure, where the involved particles are uniformly distributed. When the particles penetrate through the cube, the output data is obtained by extrapolation. This cube is equally separated into 20 sub-layers and each sub-layer is further partitioned into 16 sub-cubes (Fig.8). Each of the 320 sub-cubes can absorb a 5.9-keV photon and convert into 1640 electron/hole pairs[17].

When the photons are assimilated in the 10 bottom sub-layers of substrate, the output signals are neglected because the charge collection by the matrix is below the predefined threshold of 80 electrons, and determined by 6 times noise[8]. Thus, only the data of 10 upper sub-layers of all the epi-layer and substrate of 8–9 μm are useful for statistics and analysis.

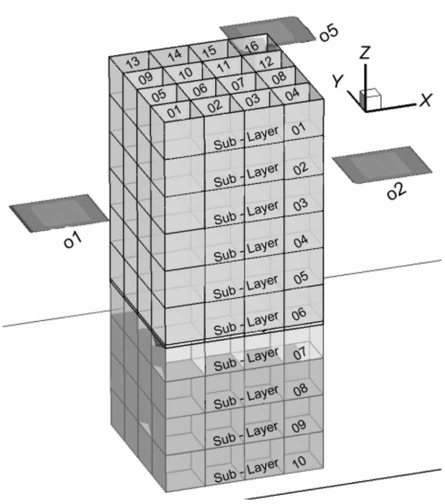

Fig.8 Schematics of the sub-layers and sub-cubes. Each of the sub-layers has 16 sub-cubes. The 10 bottom sub-layers are unnecessary.

5.1 Neighboring diffusion

The charge diffusion among the neighboring pixels is a negative effect for the digital output MAPS, because of the decreased charge collection in the seed point, leading to low signal-to-noise ratio (SNR). The fake hit rate and spatial resolution are improved by suppressing the diffusions[8]. The charges percentage is collected by each pixel (Fig.9), and up to 34%, 43% and 56% in the seed point of o5 for epi-layers of P type NR, P type HR and N type HR, respectively. Several percents of the collected charges are suppressed in other pixels.

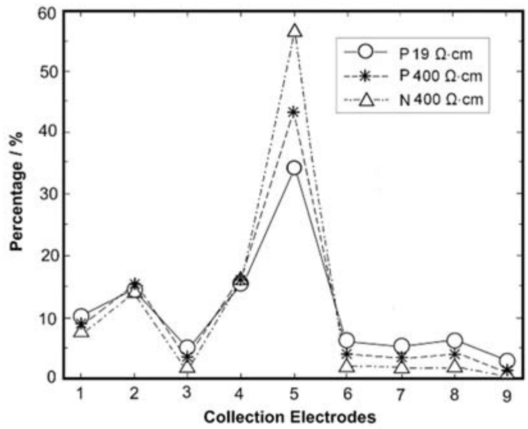

Fig.9 Percentage of collected charges by each electrode.

5.2 Collection time

Evaluating the charge collection time depends on location of the incident photon[10]. Four cubes are selected: cube 16 of sub-layer 01 (the closest to the collection electrode o5), cube 07 of sub-layer 05 (at the middle of the epi-layer), cube 01 of sub-layer 06 (the farthest position in the epi-layer), and cube 01 of sub- layer 10 (the farthest in the substrate). Table 3 gives the collection time when 90% of total charges are collected by the electrode o5. The collection time increases with the distance from the hit position to the electrode. Obviously, the N type HR epi-layer can greatly reduce the collection time due to its wide internal electric field.

5.3 Charge collection efficiency

The statistic curves in Fig.10 are achieved with the 3×3 matrix cluster. The simulation results agree well with the experiment results. The collection efficiencies can be extracted from the curves and compared with the ADC counts. A maximum (100%) of 1640 charges can be collected when a sub-cube is hit by a 5.9-keV photon of ^{55}Fe. The collection efficiency, as an important MAPS factors, is defined as the position ratio of primary peak to characteristic peak. In Fig.10, the collection efficiency is 73% for NR structures, 88% for P type HR structures and 98% for N type HR structures. The N type HR sensors are of the best collection efficiency.

Table 3 Collection time (in ns) of the sub-cubes.

Sub-layers	Sub-cubes	P 19 Ω·cm	P 400 Ω·cm	N 400 Ω·cm
01	16	1.37	1.24	1.78
05	07	116.3	52.8	23.1
06	01	144.5	74.4	33.8
10	01	181.6	122.8	77.2

In Fig.10, an interesting phenomenon is that the measured primary peak widths differ from the simulation results, due to the difference of the finite element analysis in the solver SD with the reality randomness. In the simulations, each charge behavior is definitely generated, and dominated by the Poisson equation and the electron/hole continuity equations at the given boundary and initialization. As a result, quite a few events are counted in the characteristic peak, and shape of primary peak is meaningless. On the contrary, the characteristic peak could not be found in the measurements because of the random thermal motion of non-equilibrium carrier. Fortunately, MAPS is a tracking detector for spatial discrimination rather than energy resolution. Therefore, the Matlab tool is used to get smooth curves and relative accurate positions of the primary peak.

Also, the positive effects of the charge collection are verified by another transient simulation method[18]. Briefly, the particle in a heavy ion particle model hits at the central pixel and penetrates through the virtual sensor, thus accurately impinging on quarter of the diagonal. The MIP can generate an average 80 electron/hole pairs per micrometer along the particle track. In our simulation, about 3500 electron/hole pairs generated in total depth stand for the ordinary situation of an impinging MIP[10]. Under these circumstances, the number of electrons collected in 50 ns is 1041 by the doped seed point pixel of N type HR, 413 by the N type NR; and 683 by the P type HR. In other words, by replacing the P type HR with an epi-layer N type HR, the charge collection increases by about 25%. The current outputs for the o5 electrode of seed point pixel are shown in Fig.11.

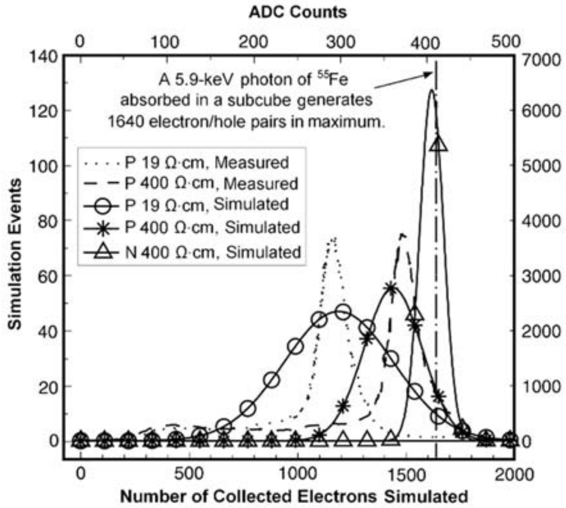

Fig.10 Charge collection efficiency of different epi-layers. The measured data (from ^{55}Fe experiments) correspond to the top and right axes. The simulated curves using Sentaurus are fitted by Matlab tool.

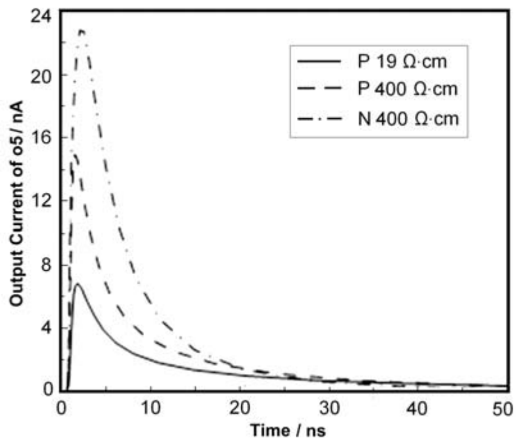

Fig.11 The current at the electrode o5 of seed point pixel.

6 Conclusion

This paper presents the simulation results about the static characteristics and charge collection performance of HR epitaxial MAPS, especially the N type ones. As a basis of the work, virtual devices of a single pixel and a 3×3 matrix are built with necessary physical models. In the static simulations, the distributions of electric potential and electric field in the N type epi-layers help the N-wells to collect the electrons. Collection performance of N type HR structures is illustrated by the transient simulation. Results show that the electron diffusion among the neighboring pixels is suppressed, increasing the collection percentage of the seed point pixel; the charge collection time in seed point decreases. Finally, the collection efficiency improving is comparable with experimental results from the real MIMOSA-26 chips. Further, the resistivity optimization needs to be carried out because several epi-layers of kΩ·cm or substrate with significant performance have been used to fabricate hybrid active pixel sensors[19,20]. Overall, the N type HR epitaxial wafer is a promising choice for MAPS detector manufacturing and collection performance improving.

Acknowledgements

We thank Christine Hu-Guo, Andrei Dorokhov and Wojciech Dulinski from Institut Pluridisciplinaire Hubert Curien, France for helping us in early stages of this work. Also, this work is supported by the France-China Particle Physics Laboratory (FCPPL) and the China Scholarship Council (CSC) grant.

References

1 Turchetta R, Berst J D, Casadei B, *et al.* Nucl Instrum Meth A, 2001, **458:** 677–689.

2 Deptuch G, Berst J D, Claus G, *et al.* IEEE Trans Nucl Sci, 2002, **49:** 601–610.

3 Ballin J A, Crooks J P, Dauncey P D, *et al.* A novel CMOS monolithic active pixel sensor with analog signal processing and 100% fill factor. IEEE Nucl Sci Sym Conf, Honolulu, US, 2007, **2:** 931–935.

4 Dulinski W, Besson A, Claus G, *et al.* IEEE Trans Nucl Sci, 2007, **54(1):** 284–289.

5 Dulinski W, Berst D, Besson A, *et al.* Radiation hardness improved CMOS sensors as particle detectors in high energy physics and medical applications. IEEE Nucl Sci Symp Conf, Portland, Oregon USA, 2003, **1:** 310–314.

6 Heini S, Himmi A, Hu-Guo C, *et al.* IEEE Trans Nucl Sci, 2009, **56:** 346–353.

7 Deptuch G, Dulinski W, Caccia M, *et al.* IEEE Trans Nucl Sci, 2005, **52:** 1745–1754.

8 Baudot J, Bertolone G, Brogna A, *et al.* First test results of MIMOSA-26, a fast CMOS sensor with integrated zero suppression and digitized output. IEEE Nucl Sci Symp Conf, Orlando, US, 2009, 1169–1173.

9 Wermes N. IEEE Trans Nucl Sci, 2004, **51(3):** 1006–1015.

10 Deptuch G, Winter M, Dulinski W, *et al.* Nucl Instrum Meth A, 2001, **465:** 92–100.

11 Buturla E M, Cottrell P E, Grossman M, *et al.* IBM J Res Dev, 1981, **25:** 218–231.

12 Sentaurus User Guide, Synopsys Inc, 2008.

13 Kalliopuska J, Eranen S, Orava R. Simulations of 3D silicon radiation detector structures in 2D and 3D. IEEE Nucl Sci Symp Conf, Puerto Rico, 2005, **2:** 803–807.

14 Pennicard D, Pellegrini G, Lozano M, *et al.* IEEE Trans Nucl Sci, 2007, **54:** 1435–1443.

15 Husson D. Nucl Instrum Meth A, 2001, **461:** 511–513.

16 Hu-Guo C. Development of fast and high precision CMOS pixel sensors for an ILC vertex detector, IPHC Workshop, France, Mar. 2010.

17 Deveaux M, Claus G, Deptuch G, *et al.* Nucl Instrum Meth A, 2003, **512:** 71–76.

18 Fu M, Tang Z, Nucl Instrum Meth A, 2011, **646:** 153–157.

19 Calvo D, De Remigis P, Osmic F, *et al.* Nucl Instrum Meth A, 2008, **594:** 29–32.

20 Chen W, De Geronimo G, Li Z, *et al.* IEEE Trans Nucl Sci, 2002, **49:** 1006–1011.